ADVANCED FUNCTIONAL MATERIALS
www.afm-journal.de

Rapid Fabrication of Soft, Multilayered Electronics for Wearable Biomonitoring

*Michael D. Bartlett, Eric J. Markvicka, and Carmel Majidi**

Soft integrated electronics are key components for emerging applications in wearable biomonitoring, soft co-robotics, and physical human–machine interaction. They are composed of soft and elastically deformable circuits and sensors that are combined with packaged microelectronics for signal processing, power regulation, and communication. While promising, widespread use of soft wearable electronics is currently limited by the lack of robust fabrication techniques to rapidly, efficiently, and precisely assemble soft and rigid components into multilayered systems. Here, an efficient digital fabrication approach is presented to create highly customizable wearable electronics through rapid laser machining and adhesion controlled soft materials assembly. Well aligned, multilayered materials are created from 2D and 3D elements that stretch and bend while seamlessly integrating with rigid components such as microchip integrated circuits, discrete electrical components, and interconnects. These techniques are applied using commercially available materials and components and the fabrication of thin, lightweight, customized sensor skins is demonstrated in under an hour. These fully integrated wireless devices conformably bond to the hand and are successfully used for monitoring hand gesture, pulse rate, and blood oxygenation. These materials and methods enable custom wearable electronics while offering versatility in design and functionality for a variety of applications through material selection and construction.

1. Introduction

Progress in the performance, multifunctionality, and accessibility of soft electronic materials has enabled wearable devices with reduced dependency on printed circuits that are rigid or inextensible. These advances have led to the emergence of deformable circuits and sensors that avoid mechanical impedance mismatch with skin by matching the elastic properties of soft biological tissue.[1,2] Applications include wearable monitoring of physiological signals, electronic skin for data entry, and skin-mounted sensors for joint proprioception and motion capture.[3–7] The ability for these electronics to bend, twist, and stretch is accomplished by using soft elastomers as a carrier medium for deterministically patterned metal wiring,[8] percolating networks of conductive nanoparticles,[9–14] grafted electrically active ionomers and conductive polymer groups,[15,16] and conductive fluids such as carbon filled grease,[17] liquid metals,[18–20] and ionic liquids.[21,22] While promising, efforts to incorporate these materials into fully integrated wearable devices are currently limited by the lack of robust and size-scalable rapid manufacturing techniques. Current methods typically require customized equipment or cleanroom fabrication, can be labor-intensive, and take hours to days to create fully functional devices. Such constraints can limit personalized configurations and slow down design iterations, which can be particularly limiting in creating devices for multiple users. These various drawbacks make it difficult to accelerate development and can be potential barriers for scalability and commercialization,[23] especially in the emerging area of personalized health monitoring.

Robust integration of soft materials into wearable computing and biomonitoring systems requires a comprehensive fabrication approach that allows for a broad range of electronic materials, substrates, circuit architectures, and surface-mounted technologies. This includes reliable methods for patterning, precision alignment, bonding, encapsulation, and electrical interfacing. The latter is particularly essential for local computation and communication,[24] energy-efficient wireless networks,[25,26] and connecting to external leads for power or signal processing.[27] Advances in rapid prototyping techniques, such as 3D printing and laser machining of soft materials, provide paths forward to achieve these objectives while accelerating design cycles and commercial development.[17,28–30] Recent work has shown how these approaches can enable the fabrication of multiple sensors at once with soft materials.[17,30] However, methods like 3D printing are limited in the mechanical and electrical performance of their build materials and do not support automated integration of integrated circuits (IC) components, which are necessary for fast, energy efficient, and miniaturized signal processing and communication.[31] This

Dr. M. D. Bartlett, Prof. C. Majidi
Soft Machines Lab
Department of Mechanical Engineering
Carnegie Mellon University
Pittsburgh, PA 15213, USA
E-mail: cmajidi@andrew.cmu.edu
E. J. Markvicka, Prof. C. Majidi
Soft Machines Lab
The Robotics Institute
Carnegie Mellon University
Pittsburgh, PA 15213, USA

DOI: 10.1002/adfm.201602733

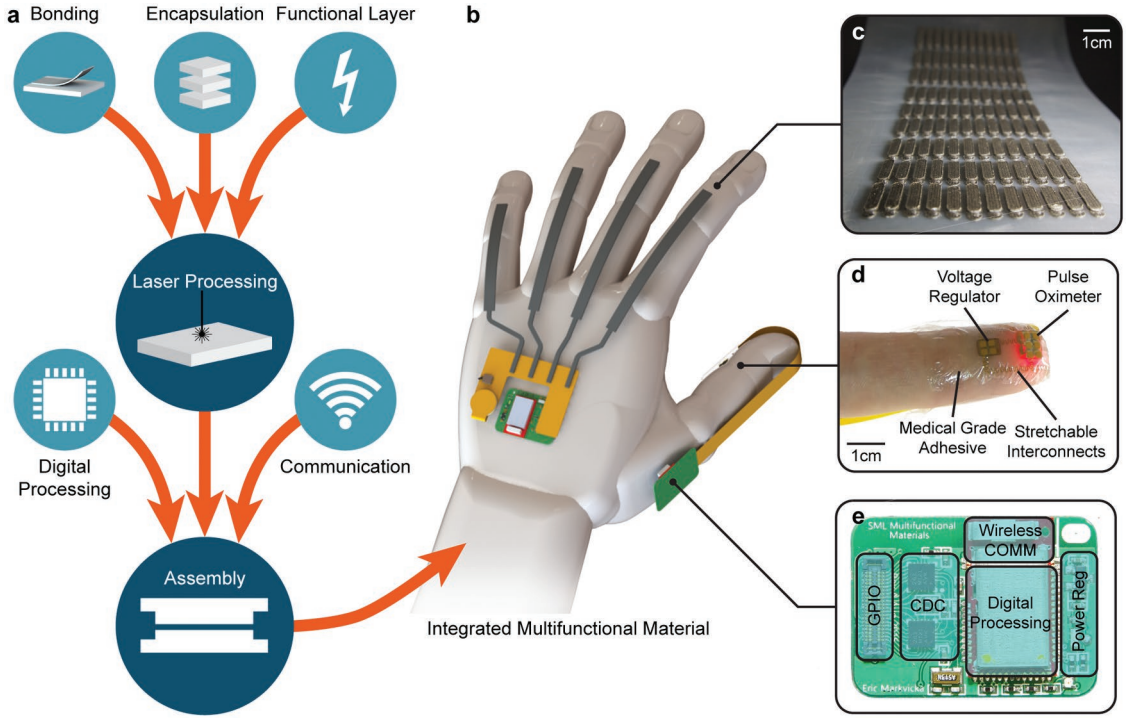

Figure 1. Multifunctional biomonitoring materials and assembly. a) Scheme for fabricating and assembling multiple functional components into an integrated system for wearable biomonitoring. b) Schematic illustration of integrated multifunctional material on a hand model.[32] c) Photograph of an array of 108 soft strain sensors created through the rapid fabrication process. d) Soft pulse oximeter mounted on a finger for wearable heart rate and peripheral oxygen saturation (SpO_2) monitoring. e) Analog and digital sensor data are collected, processed, and transmitted wirelessly through a modular, multifunctional Bluetooth Smart module.

is especially limiting for applications in wearable physiological sensing and biomonitoring that rely on packaged microchips for biosignal acquisition and processing. Salient examples of this are photoplethysmography (PPG), peripheral capillary oxygen saturation (SpO_2) and other vitals that can be obtained through optical biosensing. Therefore, the complete, sequential integration of numerous soft sensors with crucial components for communication, encapsulation, bonding or attachment layers, and stretchable electrical interconnects for power or signal processing still remains a significant challenge.

Here we show the fabrication and evaluation of numerous, completely functional wearable electronics created from commercially available films through rapid prototyping and assembly techniques that integrate multiple soft material layers and rigid elements in a single process (**Figure 1**a). We use a readily available CO_2 laser outfitted with a simple alignment system to allow for the precise assembly of sensors through deterministic, adhesion controlled soft transfer printing techniques. Assembly of the patterned material is controlled by modifying either the adhesion energy of the silicone substrate or by adjusting the laser processing conditions. The sensors do not require curing, surface modification, or additional chemical reactions and are bonded together through the inherent adhesion of the soft layers. This enables rapid fabrication that is not dependent on cure kinetics. The materials are characterized for stretchable stain sensing to over twice their original length and are shown to be stable, show little hysteresis upon cyclic loading, and are capable of being loaded over numerous cycles. This technique is extended to a UV laser system, which expands the choice of allowable materials (including thin metal film) and enables the rapid fabrication of custom stretchable electronics through deterministic architectures. We demonstrate the practical applicability of this approach with a soft, thin, and lightweight circuit that adheres to the skin and has on-board processing, power, and wireless communication for remote gesture monitoring and pulse oximetry (Figure 1b–e).

2. Results and Discussion

2.1. Fabrication Methodology

Rapid fabrication of soft functional materials is accomplished by using a combination of laser cutting with alignment control to create the individual layers and assembly of layers through the development of a soft transfer printing technique (**Figure 2**a). The materials must satisfy criteria such as (i) low effective elastic modulus, (ii) high extensibility, (iii) processable by laser cutting, and (iv) bonding compatibility. To fulfill these criteria, we chose off-the-shelf materials including insulating (VHB 4905, 3M, thickness = 0.5 mm, surface resistivity > 10^{16} Ω sq^{-1})[33] and conducting (eCAP 7850, 3M, thickness = 0.15 mm, surface resistivity = 10 Ω sq^{-1})[34] acrylic tapes. These materials are soft and highly extensible and due to their inherent adhesive characteristics provide robust adhesion upon lamination under light pressure without additional

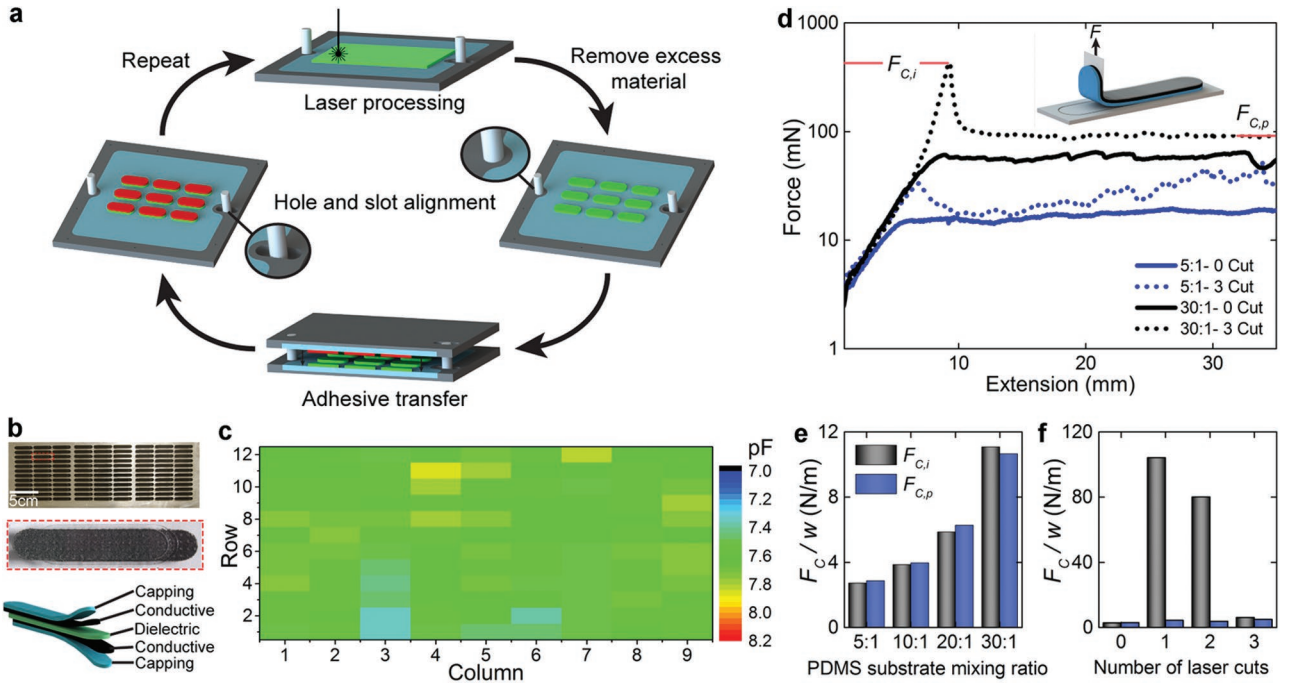

Figure 2. Deterministic adhesive assembly and characterization. a) Scheme for rapid assembly of multilayered electronics using deterministic adhesive transfer. b) Photograph of the 108 strain sensor array, a close up of an individual sensor, and a schematic showing the multilayered construction. c) Contour plot of the capacitance values of the sensor array as a function of location across the entire sheet. d) Force versus extension plot for a 90° peel experiment for two different substrates and laser processing conditions (note the y-axis is log scale). e) Normalized peel force for different mixing ratios of PDMS substrates without laser processing. f) Normalized peel force as a function of the number of laser cutting cycles on the 5:1 PDMS substrate; refer to legend in (e).

treatment. Additionally, these materials are readily available in roll form and thus offer the advantage of being easily accessible, available in large quantities, and amenable to scalable production.

To control alignment during cutting and subsequent assembly, we developed a simple alignment fixture that can be placed into a CO_2 laser cutter (30 W VLS 3.50; Universal Laser Systems). The fixture has six degrees of freedom to provide corrections in orientation and position for uniform cutting conditions across the substrate and repeatable alignment within the laser in XYZ for subsequent polydimethylsiloxane (PDMS) substrates (Figures S1 and S2, Supporting Information). Alignment is provided by mating holes and slots in the PDMS substrate with corresponding pins on the alignment fixture during cutting and on a machine table for assembly. This provides low-cost, kinematically constrained alignment with submillimeter precision.[35]

PDMS substrates (stamps) are placed on the fixture with a supporting backing featuring a machined hole and slot. The functional material to be patterned is laminated on the stamp and a custom planar design is cut (for specific settings, see Table S1, Supporting Information). Excess material is removed from the stamp after cutting and subsequent layers are then laminated onto different stamps and laser patterned. Once the patterning (cutting) is complete, the individual layers are assembled through the deterministic soft material transfer printing process using a pair of locating pins on a machine table (Figure 2a). This process allows for efficient, parallel fabrication of numerous sensors simultaneously. We demonstrate this technique by creating a batch of 108 cm scale strain sensors in under 45 min with 100% yield (Figure 2b and Video S1, Supporting Information). Further electrical characterization reveals that the sensors are nearly identical, with an average value of 7.6 ± 0.1 pF across the array of sensors, a variance of less than 2% (Figure 2c).

2.2. Soft Transfer Printing Characterization

The assembly of both rigid and soft components through an adhesion based transfer printing process is challenging due to the varying material stiffness, viscoelastic response, and interfacial properties. Previous work with transfer printing soft elastomer layers includes decal transfer lithography, which involves chemical bonding treatments and multiple steps to transfer a single layer.[36] Kinetic controlled transfer printing can be used without chemical treatments but relies on rate dependent adhesion,[37] which can be challenging with multiple rate dependent components in the system. To overcome these challenges, we accomplish material assembly by controlling the substrate adhesion energy by modifying their viscoelastic response through PDMS mixing ratio and by using laser cutting to tune adhesion response. This enables deterministic material construction in multidimensional (2D/3D) layouts. To characterize the adhesion transfer process, 90° peel experiments are conducted. The samples are prepared in the same manner as the transfer process and after removing excess sensor material, an inextensible film is adhered to the sensor and then loaded into

a peel setup. Representative peel adhesion curves for 5:1 and 30:1 (oligomer-to-curing agent ratio) substrates are presented in Figure 2d, where the force increases until crack initiation, $F_{c,i}$, and then drops as the crack begins to propagate at a constant force, $F_{c,p}$. Both the substrate choice and laser cutting conditions control the adhesion behavior and it should be noted that the y-axis is plotted on a log scale to capture the significant differences in adhesion force for the different conditions. Specifically, after three laser cuts the 30:1 substrate has an initiation force that is over 10× higher than the 5:1 substrate. This difference enables the samples to be controllably transferred from the 5:1 substrate to the 30:1 substrate.

This mechanism for adhesion control was investigated further by varying the substrate mixing ratio from 5:1 to 30:1 and the laser cutting was varied from 0 to 3 passes on the same location on the substrate. For the case where sensors are laminated onto the substrates with no laser cutting, there is an increase in peel adhesion force as the mixing ratio of the substrates increases (Figure 2e). This can be attributed to the increasing viscoelastic response of the materials as the mixing ratio increases due to greater dissipation near the crack tip.[38] Laser cutting also acts as a significant control parameter in this transfer process. As shown in Figure 2f, the peel initiation force increases by nearly 40× when a sensor is laser cut on the 5:1 substrate compared to just laminating the sensor onto the substrate. As subsequent cuts are made this initiation force decreases and on the third pass the force nearly returns to the laminated value. Optical microscopy images show that the sensor layers become impinged into the PDMS substrate upon laser cutting, which results in a greater force to separate the materials at the contact edge (Figure S3, Supporting Information). This effect is reduced upon subsequent cutting as the already formed cut line in the PDMS reduces the interaction between the sensor layers and the substrate. This result allows the substrates to be used over many fabrication cycles because the laser cutting effects diminish upon subsequent cutting and the substrate adhesion energy then dominates the transfer process. The stamp can also be preconditioned by running the laser cutter over the stamp at a reduced power and speed before the material is laminated to the stamp to diminish the impinging effect of laser cutting. This is especially important if transfer of the material (ink) is desired.

2.3. Soft Sensor Characterization

Sensor characterization is performed under tensile loading to evaluate material performance. To investigate the transient effects of these sensors we first examine the influence of strain rate. Varying the loading rate from 5 to 50 mm min^{-1}, plots of the relative capacitance C/C_0 versus strain all fall on the same line with all rates having a strain detection range over 100% strain (**Figure 3**a). In the case of the 5 mm min^{-1} loaded sample, reliable capacitance measurements are obtained for up to 150%

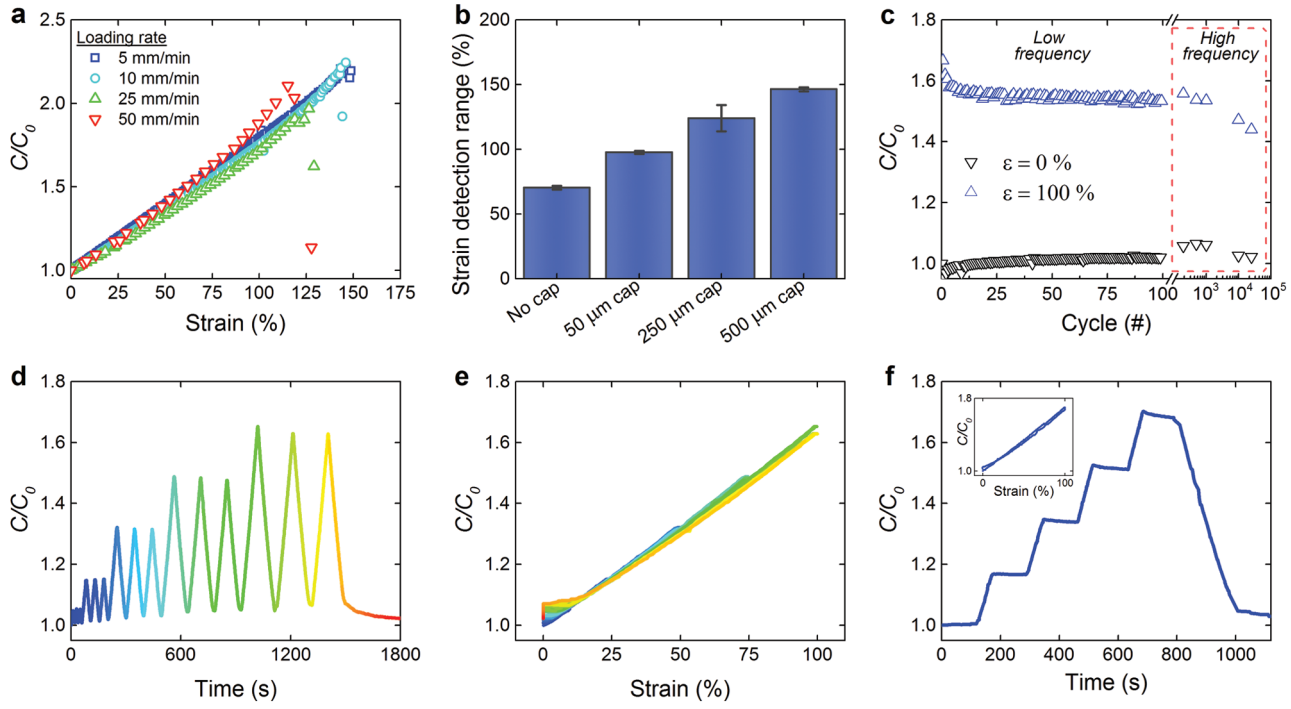

Figure 3. Soft strain sensor characterization. a) Normalized capacitance versus strain under uniaxial deformation for four different loading rates. b) The maximum strain measured by the soft sensors can be tuned by varying the thickness of supporting layers, errors bars are ±1 s.d. ($n = 3$). c) The sensors are capable of undergoing multiple loading cycles, the data points correspond to the normalized capacitance values measured at 0% and 100% strain for each loading cycle. The x-axis is plotted on a log scale after 100 cycles. d) Cyclic loading to increasing strains (10%, 25%, 50%, 75%, and 100%) plotted as a function of time and as a function of strain e), where the cooler and warmer colors represent earlier and later times, respectively. f) Sensors are subjected to a strain and hold deformation profile (25%, 50%, 75%, and 100%, strain) and display minimal drift under constant loading. The inset shows the data as a function of strain. Plots in (d), (e), and (f) are smoothed with a five-point median filter to improve data display.

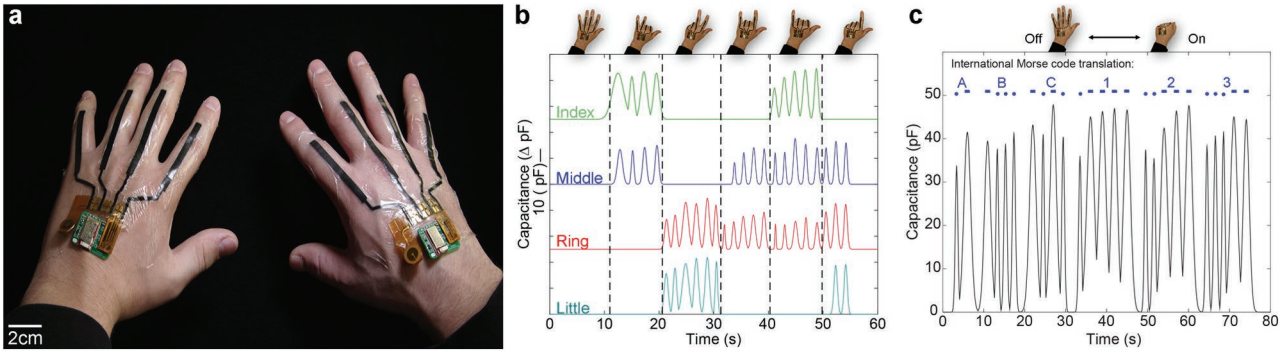

Figure 4. Wearable integrated sensing skin. a) Photograph of sensing skin mounted on the hands, where the black material is the active sensor region which extends over the metacarpophalangeal and proximal interphalangeal joints of each finger. b) Posture recognition of six different gestures on the hand. The photographs are the posture for each region. c) Communication of Morse code though the opening and closing of the hand at different time intervals to represent dots and dashes. The Morse code translation of the signal is A-B-C-1-2-3. All data in the figure are transmitted wirelessly through the BLE protocol.

strain (Figure 3a) with a gauge factor of 0.9. As the capacitance depends on the relative permittivity of the dielectric and the geometry of the sample, this result shows that the kinematics of the deformation are independent of loading rate. The capping layers (as seen in Figure 3b) are also found to have an influence on the maximum strain detection range that can be reliably measured. Referring to Figure 3b, the sensor range is observed to increase with the capping thickness. This response is attributed to a more uniform strain distribution induced by the thicker capping layer. Extended use of the sensors is characterized by performing cyclic loading up to 100% strain for 100 cycles at a frequency of 0.01 Hz. After an initial break-in period, the signal stabilizes and is repeatable for the remaining cycles (Figure 3c). Further cyclic testing was also performed at a higher rate (5 Hz) up to 25 000 cycles. The data show that the sensor response slightly decreases after 1000 cycles but is still functional at the end of the experiment showing the potential for long term use. Hysteresis is examined by performing cyclic loading experiments. The sensor is strained for three cycles at increasing levels of strain, from 10%, 25%, 50%, 75%, and 100% strain (Figure 3d). When plotting these data as a function of strain, the loading and unloading curves are indistinguishable, showing that the sensors have a very low hysteresis upon cyclic loading (Figure 3e). Lastly, the sensors are strained and then held for 120 s at increasing strains of 25%, 50%, 75%, and 100%. When held in a strained state the sensors show little signal creep. This is an advantage of capacitive sensing over resistive sensors, which can display larger degrees of signal creep (Figure 3f).[17] When looking at these data as a function of strain (Figure 3f inset), the drops in capacitance are on the order of the hysteresis of the signal and thus do not contribute any more than cyclic loading. Additionally, we find insignificant capacitive artifacts from a human hand relative to the signal generated from deformation of the sensor (Figure S4, Supporting Information). These experiments show the robust performance of the sensors over large deformations and many loading cycles.

2.4. Integrated Sensor Skin

Body mounted electronics that are designed to naturally interface with the human skin can provide inherent advantages and superior sensitivity for health monitoring compared to devices made from rigid materials.[16,39] To demonstrate the practical capabilities of the fabrication process, we produce two customizable integrated sensor skins in under an hour that adhere to the hand and monitor hand gestures. The skin contains four capacitive strain sensors that extend over the metacarpophalangeal and proximal interphalangeal joints of each finger. Stretchable circuit interconnects are used to connect the sensor elements to a flexible printed circuit (FPC) board that contains a Bluetooth transceiver and is powered with a coin cell battery (**Figure 4**a). As with the capacitive sensor electrodes, the interconnects are composed of laser-patterned eCAP 7850, which bonds to the terminals of the FPC. The fabrication of the soft integrated skin follows the methodology described in Section 2.1 with the added capability of transferring the FPC interface board onto the integrated sensing skin during the processing to ensure proper alignment. The integrated skin adheres to the hand using a medical grade, highly breathable adhesive dressing (Tegaderm, 3M). The wearable system is lightweight (less than 5 g) and thin enough to fit under an examination glove (Figure S5, Supporting Information).

The functionality of the integrated skin is shown by a series of hand gestures. As shown in Figure 4b and Video S2, Supporting Information, a variety of gestures are recognized by the integrated sensing skin. In these experiments, the fingers are cycled through different multifinger gestures, where capacitance of the individual strain sensors is measured at a frequency of 10 Hz. The signals are wirelessly transmitted to a host computer through the bluetooth low energy (BLE) protocol. The signals are then postprocessed in MATLAB (R2015b) (see Experimental Section for details). Alpha-numeric data communication is also possible through the integrated sensing skin, where Morse code can be generated by opening and closing the hand at different frequencies to generate the three communication states: dot, dash, and silence. This is demonstrated in Figure 4c, where A-B-C-1-2-3 is transmitted and is interpreted through software to automatically identify the pattern of dots and dashes. Throughout the integrated sensing skin testing, 444 finger states were recorded (finger open or finger closed). Of these, 96% of the finger states were correctly identified (see Figure S6, Supporting Information, for details). The interface

between the sensors and the FPC was also evaluated under cyclic loading. After 25 000 bend cycles, the interconnects were still functional and showed a decrease in resistance over time, showing the electrical and mechanical robustness of the integrated sensor skin (Figure S7, Supporting Information) created through our rapid fabrication process. The ability to rapidly generate wearable integrated sensing skins without the need for pattern masks enables faster design cycles and flexibility in creating custom wearables for multiple users.

2.5. Skin Mountable Pulse Oximeter Device

To extend this fabrication methodology to a wider variety of materials, we utilize a UV laser micromachining system (ProtoLaser U3; LPKF), which is capable of patterning metals in addition to polymeric materials. Instead of an alignment platform, the laser micromachining system is equipped with a fiducial recognition camera. Material assembly follows the same principals as the CO_2 laser fabrication, where alignment pegs control layer alignment, and deterministic adhesion transfer printing is used to assemble each layer into a multilayer construction. We take advantage of the additional material capabilities by laser patterning serpentine architectures of stretchable interconnects out of 70 µm thick flexible copper-clad (FR7031 DuPont) to create a wearable pulse oximeter (**Figure 5**a). This soft device is capable of bending and stretching (Figure 5c,d) and consists of a combination of soft materials and rigid components that are all sequentially assembled through the laser patterning and adhesion assembly process. During assembly of the rigid components the PDMS substrate thickness was chosen so that the lateral dimension of the rigid component was no more than twice the substrate thickness to avoid adhesion effects from substrate confinement.[40,41] The multilayer composite consists of a medical grade adhesive for bonding to the skin, laser patterned flexible copper-clad interconnects, and a through thickness conductive adhesive layer (Electrically conductive adhesive transfer tape (ECATT) 9703, 3M, thickness = 0.05 mm, contact resistance < 0.3 Ω).[42] The ECATT serves to connect the interconnects to the active and passive electrical components electrically and adhesively while preventing shorting within the plane of the circuit (Figure 5b). We take advantage of the parallel processing capabilities of the assembly process to simultaneously assemble four fully functional wearable pulse oximeter devices (Table S3, Supporting Information) in under an hour. The integration of the soft and rigid elements is robust and maintains functionality after 25 000 bend cycles to a radius of 5 mm (Figure S8, Supporting Information). The ability to assemble planar as well as 3D components of both soft and rigid elements in a parallel manner provides versatility to create a variety of functional wearable devices.

The functionality of the wearable pulse oximeter device is investigated while cycling on a stationary bicycle (Figure 5e). The pulse oximeter data are collected at a frequency of 200 Hz and transmitted wirelessly using the BLE protocol at 15 Hz. The pulse oximeter is attached to the index finger of a human subject during a graded-load exercise test in which cycling power is stepped up from 0 W at 30 s to 100 W for 60 s, increased to 200 W for 120 s, stepped back to 100 W for 60 s, and then 0 W for 30 s (Figure 5f). During this protocol heart rate and

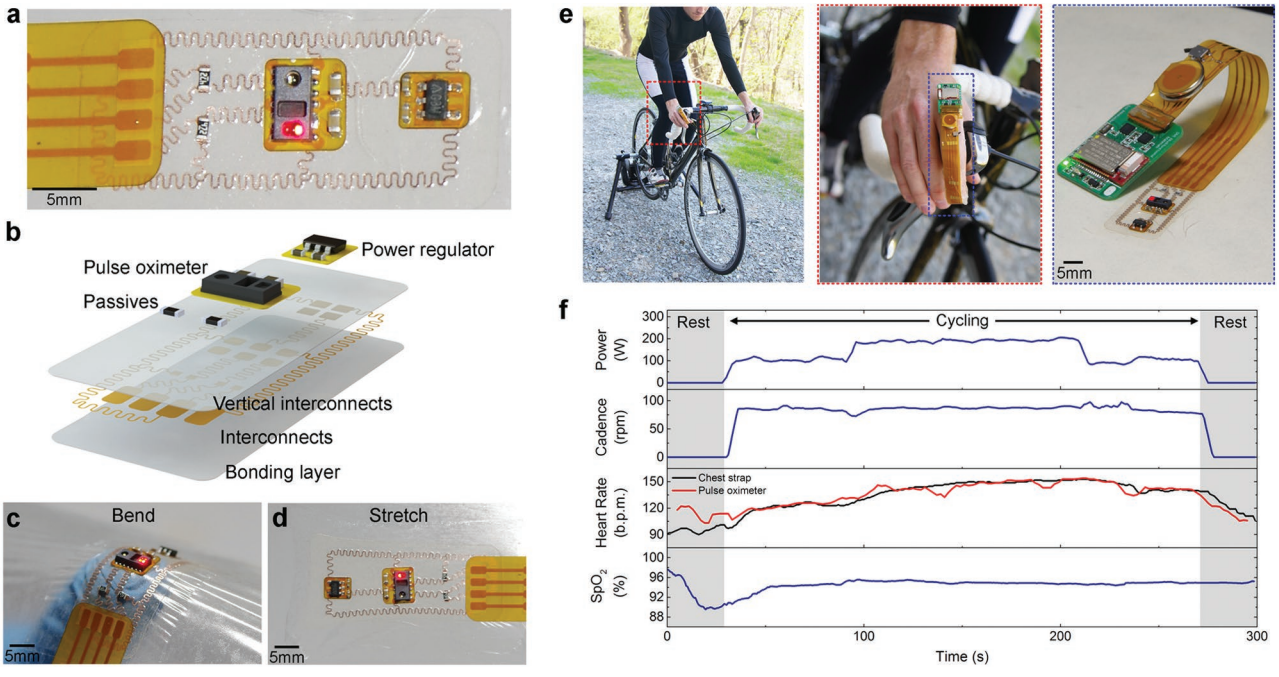

Figure 5. Wearable pulse oximeter and characterization. a) Photograph of the wearable pulse oximeter, with the red light-emitting diode (LED) illuminated. b) Schematic of the device in (a) showing the different layers and component layout. c) The pulse oximeter is capable of undergoing bending and d) stretching. e) The wearable pulse oximeter mounted on the index finger of a cyclist on a stationary bicycle. f) Data as a function of time for a graded cycling test, where power output is stepped up and down and heart rate and SpO_2 are measured with the wearable pulse oximeter. Filtered PPG signals can be found in Figure S9 (Supporting Information).

peripheral oxygen saturation (SpO_2) are continuously measured through the pulse oximeter while power and cadence are measured externally through the bicycle hub and an additional heart rate signal is captured through a chest strap. As shown in Figure 5f, heart rate increases as the power output increases, and the heart rate measured from the wearable pulse oximeter is in good agreement with the chest strap. Additionally, blood oxygen is found to vary as the subject steps cycling power up and down, as is commonly observed during exercise.[43]

3. Conclusion

We present a rapid fabrication process for soft multilayered electronics that allows for the seamless incorporation of rigid components with soft materials, enabling fully integrated, multifunctional devices. We demonstrate our efficient, highly customizable, and readily accessible process on two different laser micromachining systems at the sub-mm to cm scale. More than ten different materials (IC, discrete electrical components, and insulating and conductive soft films) are transferred using this deterministic adhesive transfer approach with varying shapes (2D/3D), sizes (0.01–100 cm^2), and materials properties (Young's modulus from ≈100 kPa to 100 GPa). Adhesion-controlled transfer was influenced by the choice of substrate (peel initiation force increases greater than 10x) and laser cutting conditions (peel initiation force increases by nearly 40x). We demonstrate the efficiency of this technique by creating a batch of 108 cm scale strain sensors in under 45 min with 100% yield (Video S1, Supporting Information) that show low signal hysteresis and signal creep during stretching. Such versatility allowed the realization of wireless, low-power, biomonitoring devices that adhere to the skin. These include a highly customizable soft integrated skin with strain sensors for gesture monitoring and a wearable pulse oximeter circuit with deterministically patterned stretchable copper interconnects. Both devices are fabricated in under 1 h, demonstrate reliable operation for greater than 4 h, and are functional weeks after initial testing. This fabrication method is applicable to a wide range of material sets, making it compatible with many materials currently used for stretchable and flexible electronics. This methodology provides a path forward for the design and optimization of devices for diverse applications, including soft robotics, electronic skins, and human–machine interfaces.

4. Experimental Section

Strain Sensor (CO_2 Laser) Fabrication and Characterization: A VLS 3.50 30 W CO_2 laser system is outfitted with a custom alignment platform (see Figures S1 and S2, Supporting Information, for details) which supports PDMS (Dow Corning Sylgard 184) substrates for laser machining. PDMS is mixed at oligomer-to-curing agent ratios of 5:1, 10:1, 20:1, and 30:1 and are cured at room temperature on a flat, level surface for 48 h and then postcured in an oven at 70 °C for 4 h. Sensor material is laminated onto the PDMS substrates and then laser cut with a predefined pattern. When placing the conductive eCAP layers the microfiber direction is orientated orthogonal to the intended primary stretching direction. After laser cutting, excess material is stripped off and any release liners are removed by cleaning the surface with isopropyl alcohol (IPA) and then adhesive tape is used to remove all release liners simultaneously. Layers are then assembled on alignment pegs that interface with a hole and slot in the substrate. Pressure is applied with a roller to ensure adhesive contact between layers and then the upper substrate is peeled off to transfer the patterned elements. Specific laser cutting conditions are provided in Tables S1 and S2 (Supporting Information).

Strain sensors were evaluated on a materials testing machine (Instron 5969) with custom 3D printed grips to hold the sample and provide electrical contact between the sample and external leads. The sensors were 18 ± 1 mm long, 6.5 mm wide, and 1.8 mm thick. Capacitance is measured with a benchtop inductance-capacitance-resistance (LCR) meter (BK Precision 889B) at a frequency of 200 KHz and a voltage of 1 V through the remote interface mode. Extension rates were 20, 10, and 5 mm min^{-1} for the 100% strain cyclic testing, hysteresis testing, and strain and hold testing, respectively. High cycle testing was performed on an orbital jigsaw (Black and Decker BDEJS600C) at 5 Hz on a setup previously described.[44]

Transfer Printing Adhesion Characterization: Adhesion behavior of the soft transfer printing process was investigated under 90° peel adhesion experiments. The samples consisted of a 0.5 mm thick VHB acrylic tape with a bonded eCAP layer to match the laser cutting conditions for the assembly process. The samples were 0.65 mm thick, had a width of 5.5 mm, and an inextensible film was bonded after laser cutting for testing. The samples were examined with a materials testing machine (Instron 5969) at an extension rate of 50 mm min^{-1} on a linear bearing to maintain a 90° angle while peeling. The test was conducted on four different PDMS (Dow Corning Sylgard 184) substrates with oligomer-to-curing agent ratios of 5:1, 10:1, 20:1, and 30:1 with the number of laser cutting passes varying from 0 to 3 as described in Section 2.2.

Integrated Sensor Skin and Capacitance Measurement: Based on the operation of the capacitance to digital converter (CDC), both electrodes of the strain sensor were routed to different channels on the CDC to provide redundancy. The raw capacitance for each channel is transmitted wirelessly at 10 Hz to the host computer using the BLE protocol. The integrated sensing skin is powered from a CR1220 Lithium coin cell battery (3 V 40 mAh). The charge/discharge current and frequency for each channel was set to 16 µA and 500 kHz, respectively.

A baseline subtraction function is first applied to the raw capacitance signal (window size: 500, step size: 100), grounding the signal and exposing the dominant peaks. The MATLAB peak finding function is used to find the local maxima and minima. A local maximum is considered to be an actuation point if the nearest local minimum on both sides of the local maximum are below zero. A Gaussian curve is then fit to all points surrounding the local maximum that are greater than 5 pF (see Figure S10, Supporting Information, for details).

Skin Mountable Pulse Oximeter and Photoplethysmogram Signal Measurement: The skin mountable device was designed using a fully integrated pulse oximeter sensor solution (Maxim MAX30100), which combines two LEDs, a photodetector, optics, and low-noise analog signal processing. To minimize the number of bus wires, the supply voltage is regulated on the skin mountable device. The pull-up resistors for the I^2C bus are also included on the device. Due to the small pad area, the pulse oximeter and voltage regulator was populated on a flexible carrier board to increase the overlap area between the device and interconnects. Decoupling capacitors were added to both carrier boards to ensure a steady voltage supply. The pulse oximeter was digitally interfaced to the Bluetooth module.

The pulse oximeter was powered from two CR1220 Lithium coin cell batteries (3 V 40 mAh). Two coin cell batteries were used to ensure 3.3 V was supplied to the device. The device was configured to collect data from the IR and red LED at 200 Hz with a pulse width of 400 µs, and LED current level of 20.8 mA with 14-bits of resolution. At 15 Hz, the raw PPG signal from the IR and red LED is combined into three 20-byte words and wirelessly transmitted to the host computer using the BLE protocol.

Bluetooth Module and Wireless Communication: The Bluetooth module was designed around a BLE system on a chip (SoC) (Nordic nRF51822) that incorporates a 32-bit Advanced RISC Machine (ARM) processor and ultralow power multiprotocol 2.4 GHz RF transceiver. The SoC

is interfaced with a pair of 12 channel CDCs (Freescale MPR121) to process the capacitive strain sensors. An ancillary power management circuit is shared across all devices to reduce overall size. A fine-pitch, low-profile board-to-board connector is used to interface to the wearable biomonitoring devices.

The BLE standard, sometimes referred to as Bluetooth Smart, was used to wirelessly transmit the data collected from the wearable biomonitoring devices. The Bluetooth module uses a Generic Attribute Profile with custom Services and Characteristics, which is configured as a peripheral device that can establish a connection with a central device such as a smartphone, tablet, or computer. Depending on the wearable biomonitoring device, multiple packets are transmitted over BLE between 10 and 15 Hz.

Pulse Oximeter (UV Laser) Fabrication: A LPKF ProtoLaser U3 UV laser micromachining system was used with camera based fiducial recognition to automatically and reliably locate the position of PDMS substrates that have fiducials machined into the substrate. The fiducials are precisely placed relative to the hole and slot that is used for alignment during the adhesive transfer process. PDMS is mixed at oligomer-to-curing agent ratios of 5:1, 10:1, and 20:1 and are cured at room temperature on a flat, level surface for 48 h and then postcured in an oven at 70 °C for 4 h. Interconnect material is laminated onto the PDMS substrates, the fiducials are automatically located, and the material is laser cut with a predefined pattern. After laser cutting, excess material is stripped off and any release liners are removed. Individual stencils were patterned out of release liner for the transfer of the rigid electrical components. Layers are then assembled on alignment pegs which interface with a hole and slot in the substrate. Pressure is applied to the top substrate to ensure adhesive contact between layers and then the upper substrate is peeled off to transfer the patterned elements. Specific laser cutting conditions are provided in Table S3 (Supporting Information).

Pulse Oximeter Experiments: The wearable pulse oximeter device was laminated onto the index finger of a test subject with medical grade adhesive (3M Tegaderm). Cycling experiments were performed on a stationary trainer (CycleOps Fluid) and pulse oximeter data are collected at 200 Hz and transmitted wirelessly using the BLE protocol at 15 Hz. Power and cadence were measured with a hub based power meter (PowerTap Pro+) and a second, chest strap heart rate monitor (Garmin) was also utilized. These signals are recorded at a frequency of 1 Hz. During the test cycling power starts at 0 W for 30 s and is then stepped up to 100 W for 60 s, increased to 200 W for 120 s, stepped back to 100 W for 60 s, and then 0 W for 30 s. Heart rate from the pulse oximeter is calculated from the maximum peak between 0.5 and 10 Hz of a fast Fourier transform (FFT) at 10 s intervals. SpO_2 is calculated by first normalizing the PPG signals by dividing by the DC offset. The maximum peak-to-peak distance per heart beat is then found and the optical density ratio (R) is calculated (the ratio of the peak-to-peak distance of the red to IR LED).[45,46] The SpO_2 can be calculated based on the empirical calibration of R. For this experiment, the linearization of the standard model for computing SpO_2 that is often used within literature was used.[46]

Supporting Information

Supporting Information is available from the Wiley Online Library or from the author.

Acknowledgements

M.D.B. and E.J.M. contributed equally to this work. The authors acknowledge support from the NASA Early Career Faculty Award (NNX14AO49G; Research Collaborator: Dr. Bill Bluethmann) and the Air Force Office of Scientific Research (AFOSR) Young Investigator Program (Mechanics of Multifunctional Materials and Microsystems; Dr. Les Lee; FA9550-13-1-0123). Sensor and mechanical characterization is performed on equipment supported through an Office of Naval Research (ONR) Defense University Research Instrumentation Program (DURIP) (Bioinspired Autonomous Systems; Dr. Tom McKenna; N00014140778).

Received: June 1, 2016
Revised: August 1, 2016
Published online: September 14, 2016

[1] T. Sekitani, Y. Noguchi, K. Hata, T. Fukushima, T. Aida, T. Someya, *Science* **2008**, *321*, 1468.
[2] M. L. Hammock, A. Chortos, B. C. K. Tee, J. B. H. Tok, Z. Bao, *Adv. Mater.* **2013**, *25*, 5997.
[3] D.-H. Kim, N. Lu, R. Ma, Y.-S. Kim, R.-H. Kim, S. Wang, J. Wu, S. M. Won, H. Tao, A. Islam, K. J. Yu, T. Kim, R. Chowdhury, M. Ying, L. Xu, M. Li, H.-J. Chung, H. Keum, M. McCormick, P. Liu, Y.-W. Zhang, F. G. Omenetto, Y. Huang, T. Coleman, J. A. Rogers, *Science* **2011**, *333*, 838.
[4] J. A. Rogers, T. Someya, Y. Huang, *Science* **2010**, *327*, 1603.
[5] M. Kaltenbrunner, T. Sekitani, J. Reeder, T. Yokota, K. Kuribara, T. Tokuhara, M. Drack, R. Schwödiauer, I. Graz, S. Bauer-Gogonea, S. Bauer, T. Someya, *Nature* **2013**, *499*, 458.
[6] W. Honda, S. Harada, T. Arie, S. Akita, K. Takei, *Adv. Funct. Mater.* **2014**, *24*, 3299.
[7] X. Liao, Q. Liao, X. Yan, Q. Liang, H. Si, M. Li, H. Wu, S. Cao, Y. Zhang, *Adv. Funct. Mater.* **2015**, *25*, 2395.
[8] S. Xu, Y. Zhang, J. Cho, J. Lee, X. Huang, L. Jia, J. a. Fan, Y. Su, J. Su, H. Zhang, H. Cheng, B. Lu, C. Yu, C. Chuang, T.-I. Kim, T. Song, K. Shigeta, S. Kang, C. Dagdeviren, I. Petrov, P. V Braun, Y. Huang, U. Paik, J. A. Rogers, *Nat. Commun.* **2013**, *4*, 1543.
[9] J. H. Kong, N. S. Jang, S. H. Kim, J. M. Kim, *Carbon N. Y.* **2014**, *77*, 199.
[10] D. J. Lipomi, M. Vosgueritchian, B. C-K. Tee, S. L. Hellstrom, J. A. Lee, C. H. Fox, Z. Bao, *Nat. Nanotechnol.* **2011**, *6*, 788.
[11] S. Yao, Y. Zhu, *Adv. Mater.* **2015**, *27*, 1480.
[12] M. Weigel, T. Lu, G. Bailly, A. Oulasvirta, C. Majidi, J. Steimle, *Proc. 33rd Annu. ACM Conf. Hum. Factors Comput. Syst. - CHI'15*, ACM, Seoul, Korea, **2015**, p. 2991.
[13] A. Charalambides, S. Bergbreiter, *J. Micromech. Microeng.* **2015**, *25*, 095009.
[14] A. Russo, B. Y. Ahn, J. J. Adams, E. B. Duoss, J. T. Bernhard, J. A. Lewis, *Adv. Mater.* **2011**, *23*, 3426.
[15] T. Yokota, P. Zalar, M. Kaltenbrunner, H. Jinno, N. Matsuhisa, H. Kitanosako, Y. Tachibana, W. Yukita, M. Koizumi, T. Someya, *Sci. Adv.* **2016**, *2*, e1501856.
[16] G. Schwartz, B. C.-K. Tee, J. Mei, A. L. Appleton, D. H. Kim, H. Wang, Z. Bao, *Nat. Commun.* **2013**, *4*, 1859.
[17] J. T. Muth, D. M. Vogt, R. L. Truby, Y. Mengüç, D. B. Kolesky, R. J. Wood, J. A. Lewis, *Adv. Mater.* **2014**, *26*, 6307.
[18] Y.-L. Park, C. Majidi, R. Kramer, P. Bérard, R. J. Wood, *J. Micromech. Microeng.* **2010**, *20*, 125029.
[19] S. Cheng, Z. Wu, *Adv. Funct. Mater.* **2011**, *21*, 2282.
[20] M. D. Bartlett, A. Fassler, N. Kazem, E. J. Markvicka, P. Mandal, C. Majidi, *Adv. Mater.* **2016**, *28*, 3726.
[21] J. Chossat, Y. Tao, V. Duchaine, Y. Park, *2015 IEEE Int. Conf. Robot. Autom.*, IEEE, Seattle, Wa, **2015**, p. 2568.
[22] J.-Y. Sun, C. Keplinger, G. M. Whitesides, Z. Suo, *Adv. Mater.* **2014**, *26*, 7608.
[23] C. Pang, G.-Y. Lee, T. Kim, S. M. Kim, H. N. Kim, S.-H. Ahn, K.-Y. Suh, *Nat. Mater.* **2012**, *11*, 795.
[24] D. Hughes, N. Correll, *Proc. - IEEE Int. Conf. Robot. Autom.*, IEEE, Hong Kong, China, **2014**, p. 1844.
[25] C. Gomez, J. Oller, J. Paradells, *Sensors* **2012**, *12*, 11734.

[26] B. Yu, L. Xu, Y. Li, *2012 IEEE Int. Conf. Inf. Autom. ICIA*, IEEE, Kuala Terengganu, Malaysia, **2012**, p. 763.
[27] M. A. McEvoy, N. Correll, *Science* **2015**, *247*, 1261689.
[28] C.-X. Liu, J.-W. Choi, *Microsyst. Technol.* **2011**, *18*, 365.
[29] H.-S. Chuang, S. T. Wereley, *J. Micromech. Microeng.* **2009**, *19*, 097001.
[30] T. Lu, L. Finkenauer, J. Wissman, C. Majidi, *Adv. Funct. Mater.* **2014**, *24*, 3351.
[31] H. Lipson, K. Melba, *Fabricated: The New World of 3D Printing*, John Wiley & Sons, Indianapolis, IN, **2013**.
[32] J. Schmit, Human Left Hand, GrabCAD (accessed: July 2016).
[33] Manufacture's Data Sheet: 3M 4905, http://multimedia.3m.com/mws/media/986695O/3m-vhb-tape-specialty-tapes.pdf (accessed: July 2016).
[34] Manufacture's Data Sheet: 3M 7850, http://multimedia.3m.com/mws/media/566536O/3mtm-electrically-conductive (accessed: July 2016).
[35] M. L. Culpepper, *Precis. Eng.* **2004**, *28*, 338.
[36] W. R. Childs, R. G. Nuzzo, *J. Am. Chem. Soc.* **2002**, *124*, 13583.
[37] M. A. Meitl, Z.-T. Zhu, V. Kumar, K. J. Lee, X. Feng, Y. Y. Huang, I. Adesida, R. G. Nuzzo, J. A. Rogers, *Nat. Mater.* **2005**, *5*, 33.
[38] A. Ghatak, K. Vorvolakos, H. She, D. L. Malotky, M. K. Chaudhury, *J. Phys. Chem. B* **2000**, *104*, 4018.
[39] X. Wang, Y. Gu, Z. Xiong, Z. Cui, T. Zhang, *Adv. Mater.* **2014**, *26*, 1336.
[40] M. D. Bartlett, A. J. Crosby, *Langmuir* **2013**, *29*, 11022.
[41] M. D. Bartlett, A. J. Crosby, *Mater. Horiz.* **2014**, *1*, 507.
[42] Manufacture's Data Sheet: 3M 9703, http://multimedia.3m.com/mws/media/66235O/3m-electrically-conductive-adhesive-transfer-tape-9703.pdf (accessed: July 2016).
[43] B. Rowell, L. Taylor, S. Carlson, *J. Appl. Physiol.* **1964**, *19*, 284.
[44] S. A. Pendergraph, M. D. Bartlett, K. R. Carter, A. J. Crosby, *ACS Appl. Mater. Interfaces* **2012**, *4*, 6640.
[45] M. W. Wukitsch, M. T. Petterson, D. R. Tobler, J. A. Pologe, *J. Clin. Monit.* **1988**, *4*, 290.
[46] J. M. Goldman, M. T. Petterson, R. J. Kopotic, S. J. Barker, *J. Clin. Monit. Comput.* **2000**, *16*, 475.